

# Characterization of High Thermal Conductivity Carbon Fibers and a Self-Reinforced Graphite Panel

1 September 1998

Prepared by

P. M. ADAMS, H. A. KATZMAN, and G. S. RELICK,  
Mechanics and Materials Technology Center

G. W. STUPIAN  
Electronics Technology Center

Technology Operations

Prepared for

SPACE AND MISSILE SYSTEMS CENTER  
AIR FORCE MATERIEL COMMAND  
2430 E. El Segundo Boulevard  
Los Angeles Air Force Base, CA 90245

Engineering and Technology Group

APPROVED FOR PUBLIC RELEASE;  
DISTRIBUTION UNLIMITED

19990319 009

This report was submitted by The Aerospace Corporation, El Segundo, CA 90245-4691, under Contract No. F04701-93-C-0094 with the Space and Missile Systems Center, 2430 E. El Segundo Blvd., Los Angeles Air Force Base, CA 90245. It was reviewed and approved for The Aerospace Corporation by S. Feuerstein, Principal Director, Mechanics and Materials Technology Center.

This report has been reviewed by the Public Affairs Office (PAS) and is releasable to the National Technical Information Service (NTIS). At NTIS, it will be available to the general public, including foreign nationals.

This technical report has been reviewed and is approved for publication. Publication of this report does not constitute Air Force approval of the report's findings or conclusions. It is published only for the exchange and stimulation of ideas.

  
Peter Bissegger  
SMC/AXES

**REPORT DOCUMENTATION PAGE**Form Approved  
OMB No. 0704-0188

Public reporting burden for this collection of information is estimated to average 1 hour per response, including the time for reviewing instructions, searching existing data sources, gathering and maintaining the data needed, and completing and reviewing the collection of information. Send comments regarding this burden estimate or any other aspect of this collection of information, including suggestions for reducing this burden to Washington Headquarters Services, Directorate for Information Operations and Reports, 1215 Jefferson Davis Highway, Suite 1204, Arlington, VA 22202-4302, and to the Office of Management and Budget, Paperwork Reduction Project (0704-0188), Washington, DC 20503.

1. AGENCY USE ONLY (Leave blank)		2. REPORT DATE 1 September 1998	3. REPORT TYPE AND DATES COVERED	
4. TITLE AND SUBTITLE Characterization of High Thermal Conductivity Carbon Fibers and a Self-Reinforced Graphite Panel			5. FUNDING NUMBERS F04701-93-C-0094	
6. AUTHOR(S) P. M. Adams, H. A. Katzman, G. S. Rellick, and G. W. Stupian				
7. PERFORMING ORGANIZATION NAME(S) AND ADDRESS(ES) The Aerospace Corporation Technology Operations El Segundo, CA 90245-4691			8. PERFORMING ORGANIZATION REPORT NUMBER TR-98(8565)-11	
9. SPONSORING/MONITORING AGENCY NAME(S) AND ADDRESS(ES) Space and Missile Systems Center Air Force Materiel Command 2430 E. El Segundo Boulevard Los Angeles Air Force Base, CA 90245			10. SPONSORING/MONITORING AGENCY REPORT NUMBER SMC-TR-99-05	
11. SUPPLEMENTARY NOTES				
12a. DISTRIBUTION/AVAILABILITY STATEMENT Approved for public release; distribution unlimited			12b. DISTRIBUTION CODE	
13. ABSTRACT (Maximum 200 words) Extremely high thermal conductivity graphitic materials from mesophase pitch precursors (K-1100 fibers, four experimental high thermal conductivity fibers, and a ThermalGraph <sup>®</sup> panel) were examined utilizing X-ray diffraction (XRD) and high-resolution field emission (FE) scanning electron microscopy (SEM). Of the four experimental fibers, two were produced from Amoco's standard petroleum pitch, and two were produced from an Amoco experimental pitch precursor. The low <i>d</i> -spacings, narrow peaks, and presence of three-dimensional reflections in the XRD patterns of the five fibers and the ThermalGraph <sup>®</sup> panel indicate that they are all highly graphitic. The thermal conductivities of these materials correlate best with the graphite inter-basal-plane spacing ( <i>d</i> <sub>002</sub> ). All of the materials studied appear very graphitic in high-resolution SEM micrographs of their transverse fracture surfaces. Well-developed graphene layer planes are clearly seen. High-resolution SEM examination of the ThermalGraph <sup>®</sup> panel shows that the precursor fibers have coalesced into a continuous three-dimensional structure. The result of this fiber fusion is a "self-reinforced," graphitic structure.				
14. SUBJECT TERMS Carbon fibers, mesophase pitch, scanning electron microscopy (SEM), X-ray diffraction, Thermal conductivity			15. NUMBER OF PAGES 13	
			16. PRICE CODE	
17. SECURITY CLASSIFICATION OF REPORT UNCLASSIFIED	18. SECURITY CLASSIFICATION OF THIS PAGE UNCLASSIFIED	19. SECURITY CLASSIFICATION OF ABSTRACT UNCLASSIFIED	20. LIMITATION OF ABSTRACT	

## Contents

1. INTRODUCTION .....	1
2. MATERIALS .....	1
2.1 Mesophase-based fibers.....	1
2.2 ThermalGraph <sup>®</sup> panel .....	2
3. EXPERIMENTAL .....	2
3.1 X-ray diffraction .....	2
3.2 Scanning electron microscopy .....	3
4. RESULTS AND DISCUSSION .....	3
4.1 X-ray diffraction .....	3
4.2 Scanning electron microscopy .....	5
5. SUMMARY AND CONCLUSIONS.....	11
REFERENCES.....	11
APPENDIX A .....	13

## Figures

1. Thermal conductivity vs $L_a$ for fibers and ThermalGraph <sup>®</sup> .....	4
2. Thermal conductivity vs $L_c$ for fibers and ThermalGraph <sup>®</sup> .....	4
3. Thermal conductivity vs $d_{002}$ for fibers and ThermalGraph <sup>®</sup> .....	4
4. Thermal conductivity vs $d_{002}$ for PAN and pitch fibers and ThermalGraph <sup>®</sup> .....	5
5. FE SEM photomicrographs of fractured fibers .....	6
6. FE SEM photomicrographs of the transverse fracture surfaces of standard pitch precursor fibers .....	6
7. FE SEM photomicrographs of the transverse fracture surfaces of experimental pitch precursor fiber E2 .....	7

8. FE SEM photomicrographs of the transverse fracture surfaces of K-1100 fibers.....	7
9. FE SEM photomicrographs of the open-wedge feature in fiber P1.....	8
10. FE SEM photomicrographs of the scroll structure in fiber E2.....	8
11. FE SEM photomicrographs of the corrugated structure.....	8
12. FE SEM photomicrographs of the K-1100 fiber core.....	8
13. FE SEM photomicrographs of the transverse fracture surface of ThermalGraph <sup>®</sup> panel..	9
14. FE SEM photomicrographs of the transverse fracture surface of ThermalGraph <sup>®</sup> panel..	9
15. FE SEM photomicrographs of the exposed fiber surface in ThermalGraph <sup>®</sup> panel .....	9
16. FE SEM photomicrographs of the K-1100 fiber surface.....	10
17. FE SEM photomicrographs of the internal surfaces of the K-1100 fiber.....	10
18. FE SEM photomicrographs of the internal surface of the K-1100 fiber at higher magnification and 2-kV electron beam voltage.....	10

## Tables

1. Properties of the fibers studied.....	2
2. Properties of ThermalGraph <sup>®</sup> panel .....	2
3. Summary of XRD data.....	3
4. ThermalGraph <sup>®</sup> panel XRD ply angles and preferred orientation .....	4

## 1. INTRODUCTION

Recently, new techniques for the production of extremely high thermal conductivity graphitic materials from mesophase pitch have been developed [1,2]. In these techniques, mesophase pitch is extruded through spinnerets to form filaments that can then be thermoset and heat treated in an inert environment to produce highly graphitic fibers. The extruded mesophase pitch filaments can also be formed into panels before thermosetting and heat treating, resulting in a self-reinforced graphitic product. The manufacturer, Amoco Performance Products, Inc., Alpharetta, Georgia, has designated the family of high thermal conductivity fibers as "K" fibers and the self-reinforced panels as ThermalGraph®. The high thermal conductivity of these materials is a result of their very high degree of graphitization, relatively large crystallite sizes and near-perfect crystallite alignment. Whereas the physical, mechanical and thermal properties of various pitch-based materials have been investigated, detailed characterizations of the microstructures of K fibers and ThermalGraph® have not yet been reported. In this paper, we have investigated K-1100 fibers, four experimental high thermal conductivity fibers, and a ThermalGraph® panel utilizing X-ray diffraction (XRD) and high resolution scanning electron microscopy (SEM). Our objective was to correlate XRD

parameters and microstructural features with reported thermal conductivities.

## 2. MATERIALS

### 2.1 *Mesophase-based fibers*

Five variations of mesophase-based fibers were provided to us by Amoco. All of the fibers were provided in 2000 filament tows. The K-1100 came from one particular lot of fibers. The other four fiber samples were experimental and were included in our study because their thermal conductivities had been accurately measured. Two of the experimental fiber samples were produced from Amoco's standard petroleum pitch, and two were produced from an Amoco experimental pitch precursor. One sample from each of the precursors was heat treated to a temperature of approximately 3000°C, and the remaining two samples were exposed to a final heat treatment temperature (HTT) of approximately 2650°C. None of the fiber surfaces were subjected to the usual mild oxidation normally done to improve the shear properties of composites fabricated from carbon fibers. The room temperature electrical resistivities and thermal conductivities of the experimental fibers were measured at Amoco. The thermal conductivity of the K-1100 was not measured directly, but rather was estimated by Amoco from the measured electrical resistivity. Table I presents a summary of the processing conditions for the fibers and their measured electrical and thermal conductivities.

Table 1. Properties of the fibers studied

Fiber designation	K-1100	P1	P2	E1	E2
Pitch precursor	Standard	Standard	Standard	Experimental	Experimental
Graphitization temperature (°C)	~3000	~3000	~2650	Same as P1	Same as P2
Electrical resistivity ( $\mu\Omega \cdot m$ )	1.35*	1.40	1.81	1.05	1.49
Thermal conductivity ( $W m^{-1}K^{-1}$ )	884†	862	661	1060	746

\*This K-1100 fiber lot is outside the current electrical resistivity specification range of 1.1–1.3  $\mu\Omega \cdot m$  for K-1100 fibers. It was made before the current specification went into effect.

†Estimated from electrical resistivity.

## 2.2 ThermalGraph<sup>®</sup> panel

ThermalGraph<sup>®</sup> panels are formed by winding melt-spun mesophase filament tows (2000 filaments per tow) on a bobbin with a variable wind angle. The fiber tows are then cut from the bobbin and pressed into a flat mat. The compacted mat is then thermoset and, after thermosetting, is hot-pressed at ~3000°C in an inert atmosphere to densify and graphitize the panels. The longitudinal and transverse thermal conductivities of the panels can be tailored by controlling the relative orientations of the fiber bundles within the panels. The density can be varied by controlling the amount of compaction before and during heat treatment. Volume fractions of the graphitized panels are calculated as the ratio of the panel bulk density to standard K-1100 graphite fiber density ( $2.2 g cm^{-3}$ ).

An experimental ThermalGraph<sup>®</sup> panel made by Amoco was provided to us by Research Opportunities, Inc., Torrance, California. The panel was a flat plate, 2 cm square and 4 mm thick, with a wind angle of  $\pm 5^\circ$ . The room temperature thermal conductivity of the panel was measured by Research Opportunities using a Fourier method to analyze the thermal gradient from a known heat flux [3]. Table 2 shows the reported properties of the panel studied. The intrinsic thermal conductivity of the fibers was approximated by dividing the panel thermal conductivity by the product of the cosine of  $5^\circ$  and the fiber volume fraction.

## 3. EXPERIMENTAL

### 3.1 X-ray diffraction

Wide angle  $\theta$ - $2\theta$  XRD scans were performed using Cu K $\alpha$  radiation on a computer-controlled Philips Electronics Instruments vertical powder diffractometer (APD 3720) equipped with a  $\theta$  compensating slit, a diffracted-beam graphite crystal monochroma-

tor and a scintillation detector. Samples were prepared for XRD analysis by grinding in an agate mortar and pestle. Grinding was done under acetone in order to minimize damage [4]. The powdered samples were pressed into a 100  $\mu m$  deep cavity in a standard Philips sample holder that was backed with a zero background plate. This plate consists of a single crystal of quartz that has been cut  $6^\circ$  from the  $c$ -axis and produces no XRD reflections and very little background scattering. This sample holder, with a very shallow cavity, was used because X-rays penetrate very deeply into carbon due to its low  $Z$  and density. It has been shown that "transparency" and other corrections for Compton scattering are necessary for accurate determination of peak locations and full width at half maximums (FWHMs) from thick carbon samples [5,6]. The use of very thin samples obviates the need for these corrections.

Survey  $\theta$ - $2\theta$  scans of the powders (of fibers and the ThermalGraph<sup>®</sup> panel) were run between  $2^\circ$  and  $100^\circ$  with a  $2\theta$  step size of  $0.02^\circ$ . In order to obtain more accurate measurements of the  $d$ -spacings of the graphite reflections, a small amount of NIST silicon standard (SRM 640b) was mixed with a portion of the powders. A sample of NIST LaB<sub>6</sub> line profile standard (SRM 660) was also analyzed under identical conditions in order to measure the instrumental contribution to line profile broadening. This process is required for accurate estimation of  $L_c$  and  $L_a$  from the Scherrer equation [7].  $L_c$  and  $L_a$  were calculated from the FWHMs of the (002) and (110) reflections, respectively. In calculating  $L_a$ , a value of  $K=0.90$  was used in the Scherrer equation because of the highly graphitic nature and three-dimensional crystallinity of these materials [8].

The (002) preferred orientations in the  $XY$  and  $XZ$  planes of the ThermalGraph<sup>®</sup> panel were also determined by XRD. ( $X$  is the longitudinal direction,  $Y$  is the transverse direction and  $Z$  is the through-the-thickness direction.) In addition to measuring the variation in orientation within the fiber tows,  $XY$  plane XRD orientation measurements also can be used to determine the ply angles between tows if several cross tows can be analyzed simultaneously. The panel was analyzed with a flat-plate camera employing pinhole collimation (200  $\mu m$  diameter), a sample-to-film distance of 5 cm, and nickel-filtered copper radiation. The preferred orientation of the

Table 2. Properties of ThermalGraph<sup>®</sup> panel

Pitch precursor	Standard
Layup	$\pm 5^\circ$
Fiber volume fraction	0.82
Longitudinal thermal conductivity of panel ( $W m^{-1}K^{-1}$ )	746
Calculated intrinsic fiber thermal conductivity ( $W m^{-1}K^{-1}$ )	913

basal planes in the panels was expressed by the parameter  $Z$ , which is defined as the FWHM of the azimuthal intensity profile of the carbon (002) reflection. Details of the digitization and quantification procedures used to determine  $Z$  from the flat-plate photographs are given in ref. [9].

### 3.2 Scanning electron microscopy

Transverse fracture surfaces of the fibers and of the ThermalGraph<sup>®</sup> panel were examined with a high resolution JEOL JSM-6401F field emission (FE) SEM operated at 2 to 5 kV. FE SEM allows the use of lower electron energies than conventional SEM [10]. These lower energies minimize penetration of the samples by the electron beam, thereby permitting better resolution of the features of interest.

Because of the lower chamber pressure used in FE SEM, fiber tows were prepared for examination utilizing a carbonized resin to eliminate outgassing. Two-centimeter lengths of fiber tows were infiltrated with polyarylacetylene resin [11-13] by a simple drip-coating process. These samples were cured at 250°C for 2 hours and then carbonized at 1170°C for 10 hours to drive off all volatiles and to make the matrix electrically conductive. They were then fractured under liquid nitrogen to minimize ductile fracture, and the uncoated fracture surfaces were examined directly in the FE SEM. The ThermalGraph<sup>®</sup> sample was prepared for examination by cutting a 2 mm × 2 mm × 15 mm "stick" from the panel with a slow speed diamond saw. This stick was then fractured by bending under liquid nitrogen.

## 4. RESULTS AND DISCUSSION

### 4.1 X-ray diffraction

Table 3 presents a summary of XRD  $d$ -spacing results and the crystallite sizes calculated from the instrumentally corrected FWHM values for all of the samples studied. Based on several duplicate analyses,  $d$ -spacings were very reproducible, with variations either being undetectable, or on the order of

$\pm 0.0002 \text{ \AA}$  for reflections other than (100)/(101). These latter reflections showed a variation of about  $\pm 0.001 \text{ \AA}$ , because the positions were difficult to locate using peak deconvolution and the broad (100)/(101) peak could not easily be separated into two distinct reflections. The FWHMs presented in Table 3 are for the  $K\alpha_1$  peaks, uncorrected for instrument broadening. The FWHMs of the reflections were generally reproducible to within  $\pm 0.01$ – $0.02^\circ$  for (002), (004) and (110), with slightly larger variations in the other reflections. A variation in FWHM on the order of  $\pm 0.01^\circ$  equates to an error in crystallite size of approximately  $\pm 50 \text{ \AA}$  for  $L_c$  and  $\pm 100 \text{ \AA}$  for  $L_a$  in Table 3. As discussed by Nysten *et al.* [14], measurements of  $L_a$  by X-ray line broadening incur very large uncertainties for values of  $L_a$  approaching 1000 Å, because contributions due to instrumental line broadening become very large for such narrow diffraction peaks.

The (002)  $d$ -spacings of the experimental fibers range from 3.364 to 3.372 Å, which compares with 3.366 and 3.353 Å for K-1100 fibers and single crystal graphite, respectively. The (002)  $d$ -spacing for the ThermalGraph<sup>®</sup> panel was found to be 3.364 Å, a value as low as that found for the most graphitic experimental fiber (E1) that was studied. The  $L_a$ 's of the four experimental fibers ranged from 415 to 1020 Å, while  $L_c$ 's ranged from 410 to 660 Å. These values compare with  $L_a$  of 1095 Å and  $L_c$  of 625 Å found for K-1100. The crystallite sizes ( $L_a$ ,  $L_c$ ) for the ThermalGraph<sup>®</sup> sample are 990 and 710 Å, respectively.

The low  $d$ -spacings, narrow peaks and presence of three-dimensional ( $hkl$ ) reflections in the five fibers and the ThermalGraph<sup>®</sup> panel indicate that they are all highly graphitic. The XRD data show that at the same HTT, the fibers produced from the experimental pitch precursor are more graphitic than those produced from the standard petroleum pitch precursor. This can be most easily seen in the  $d$ -spacings and FWHMs of the higher order (004) and (006) reflections. In each case, at a given HTT, the  $d$ -spacings

Table 3. Summary of XRD data\*

Fiber	K-1100	P1	P2	E1	E2	ThermalGraph <sup>®</sup>
Reflection						
(002)	3.366 (0.23)	3.368 (0.26)	3.372 (0.30)	3.364 (0.22)	3.368 (0.25)	3.364 (0.23)
(100)	2.128 (0.19)	2.128 (0.22)	2.127 (0.25)	2.128 (0.23)	2.127 (0.25)	2.128 (0.22)
(101)	2.034 (1.1)	2.036 (1.3)	2.045 (1.7) <sup>†</sup>	2.040 (1.6) <sup>†</sup>	2.042 (2.0) <sup>†</sup>	2.034 (1.2) <sup>†</sup>
(004)	1.683 (0.40)	1.684 (0.46)	1.686 (0.54)	1.682 (0.39)	1.684 (0.47)	1.681 (0.37)
(110)	1.230 (0.21)	1.230 (0.26)	1.230 (0.25)	1.230 (0.21)	1.230 (0.30)	1.230 (0.23)
(112)	1.1558 (1.04)	1.1556 (1.23)	1.1569 (1.1) <sup>‡</sup>	1.1556 (1.27)	1.1563 (1.5) <sup>‡</sup>	1.1556 (0.91)
(006)	1.1214 (0.60)	1.1219 (0.77)	1.1231 (1.01)	1.1211 (0.59)	1.1222 (0.78)	1.1207 (0.53)
$L_a$ (Å)	1095	710	770	1020	415	990
$L_c$ (Å)	625	510	410	660	505	710

\* $d$ -spacings (Å) and FWHMs in parentheses (deg  $2\theta$ ).

<sup>†</sup>Very broad and indistinct.

<sup>‡</sup>Very weak.

and FWHMs of the peaks from the experimental pitch precursor fibers are smaller and narrower than those from the standard petroleum pitch precursor fibers.

The preferred orientation and ply angle measurements from the ThermalGraph<sup>®</sup> panel are presented in Table 4. Since the average ply angle measured in the *XY* plane is  $4.9 \pm 0.5^\circ$ , and the nominal ply angle is  $\pm 5^\circ$ , it appears that XRD can be used to measure the ply angle in these materials. However, the actual area measured is very small ( $0.2 \text{ mm} \times 0.8 \text{ mm}$  long) and may not be representative of the specimen as a whole. The azimuthal FWHM of the (002) reflection within individual fiber bundles in the *XY* plane of the ThermalGraph<sup>®</sup> sample averages  $5.7 \pm 0.5^\circ$ . In contrast, the FWHM of an individual K-1100 fiber is on the order of  $0.5\text{--}1.0^\circ$ . Individual fibers or small ( $< 50 \mu\text{m}$  diameter) fiber bundles separated from the ThermalGraph<sup>®</sup> sample produced FWHMs similar to those of single K-1100 fibers, so that it appears that the misorientation is mainly due to fiber misalignment within the bundles. The preferred orientation in the *XZ* plane was found to be  $5.8 \pm 1.0^\circ$ . This value may be an indication of how much the fiber bundles are forced out of the *XY* plane as a result of bundle crossing. Alternatively, since this value is similar to that found in the *XY* plane, it may also indicate fiber misalignment within the bundles.

It is now well accepted that the thermal conductivity (*K*) of single crystal and polycrystalline forms of graphite at temperatures in the range of 200 to 1000 K is dominated by phonons (lattice vibrations). Thermal transport via phonons is limited by two principal mechanisms: scattering at crystallite grain boundaries, and scattering at point defects within the layer planes. The first mechanism is closely associated with the crystallite size  $L_a$ ; the second is less straightforward to assess. Kelly, who is principally responsible for the development of the theory of graphite thermal conductivity [15–18], has shown that the second mechanism can be approximated by treating it as a special case of isotope scattering. He has also shown that the large amount of data on irradiation-induced defects in graphite is consistent with this approach [15].

Figures 1–3 show plots of the thermal conductivities of the five fibers and the intrinsic conductivity of the ThermalGraph<sup>®</sup> (TG) panel versus  $L_a$ ,  $L_c$  and  $d_{002}$ , respectively. The lines drawn on the figures were determined by a linear least-squares approximation.

Table 4. ThermalGraph<sup>®</sup> panel XRD ply angles and preferred orientation

	Measured $\pm$ ply angle (deg)	(002) Azimuthal FWHM (deg)
<i>XY</i> plane (area #1)	$4.3 \pm 0.2$	$5.2 \pm 0.3$
<i>XY</i> plane (area #2)	$5.4 \pm 0.3$	$6.2 \pm 0.8$
<i>XZ</i> plane	-	$5.8 \pm 1.0$

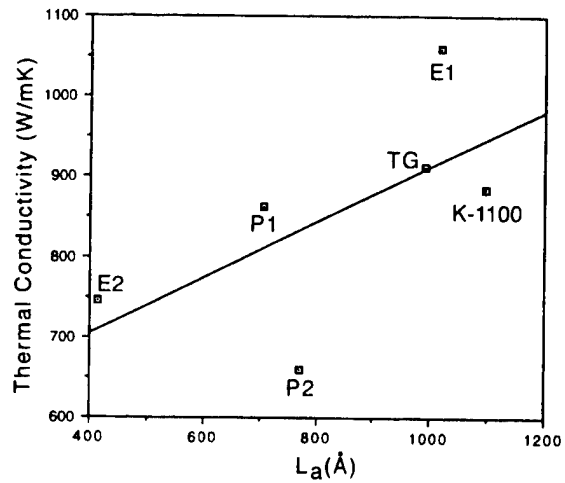


Fig. 1. Thermal conductivity vs  $L_a$  for fibers and ThermalGraph<sup>®</sup>.

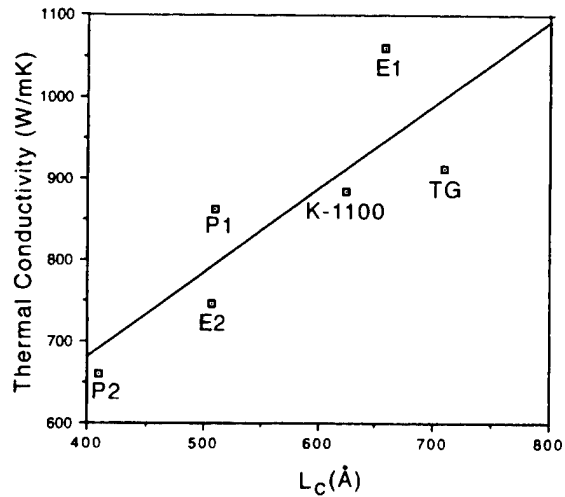


Fig. 2. Thermal conductivity vs  $L_c$  for fibers and ThermalGraph<sup>®</sup>.

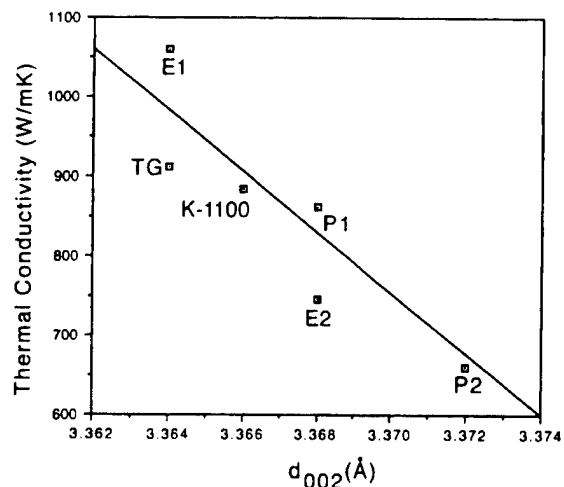


Fig. 3. Thermal conductivity vs  $d_{002}$  for fibers and ThermalGraph<sup>®</sup>.

Correlation coefficients for these lines are 0.4, 0.7 and 0.8 for Figs 1–3, respectively. From the figures, it can be seen that the thermal conductivities correlate best with  $d_{002}$  and worst with  $L_a$ . The poor correlation with  $L_a$  may in part reflect the difficulty in measuring  $L_a$  by X-ray line broadening for  $L_a$  values approaching 1000 Å, as discussed previously. Very good correlations between thermal conductivity and  $L_a$  have been reported in the past [17]. However, these correlations appear to have always been with extremely well-graphitized materials with  $L_a$  values of the order of tens of thousands of ångströms, where  $L_a$  was obtained from electrical resistivity measurements, not XRD [19].

Heremans *et al.* [20] have also found a much better correlation of carbon fiber thermal conductivity with  $c$ -axis properties for a range of PAN, CVD and pitch-based fibers. In Fig. 4, we have constructed a composite plot of  $K$  versus  $d_{002}$  for the five fibers and the ThermalGraph® panel that we studied, those from ref. [20], a series of DuPont mesophase-pitch-based E fibers [14] and a series of mesophase-pitch-based P-fibers from Amoco [21]. The general trend of increasing  $K$  with decreasing  $d_{002}$  is not unexpected, as Nysten *et al.* [14] point out, because improved layer plane stacking is consistent with the removal of point-defect scattering centers such as vacancies, interstitials and impurities. In addition, of all the crystallographic parameters of interest,  $d_{002}$  can be measured the most accurately. Since we might well expect some correlation between crystallite growth in the direction of the  $a$ - and  $c$ -axes, it may be that  $d_{002}$  is a reliable indicator of  $L_a$  in this region, where measurement of  $L_a$  by XRD is subject to such large uncertainty.

The data of Fig. 4 are also seen to be sensible when plotted as two distinct linear regimes. In the low  $K$  regime, large decreases in  $d$ -spacing down to

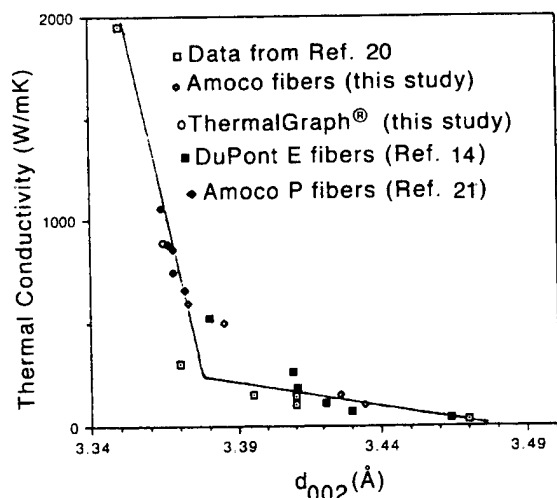


Fig. 4. Thermal conductivity vs  $d_{002}$  for PAN and pitch fibers and ThermalGraph®.

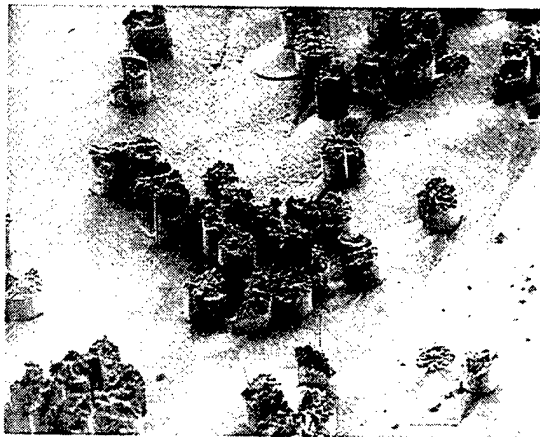
about 3.38 Å have little effect on  $K$ . We believe that in this regime, the structure is essentially turbostratic, and defects greatly limit thermal transport. From 3.38 Å down to 3.35 Å, removal of defects has a dramatic effect on  $K$ , leading to the near-theoretical value of  $1950 \text{ W m}^{-1} \text{ K}^{-1}$  for a CVD fiber heat treated to  $3000^\circ\text{C}$  [20]. It is of some interest that mesophase fibers to date have not achieved  $d$ -spacings much below those reported here ( $\sim 3.364$  Å), in spite of heat treatments of the same magnitude as that of the CVD fiber. This may be an inherent limitation imposed by geometric constraints on the layer plane stacking in such small diameter (7–10  $\mu\text{m}$ ) filaments during graphitization.

#### 4.2 Scanning electron microscopy

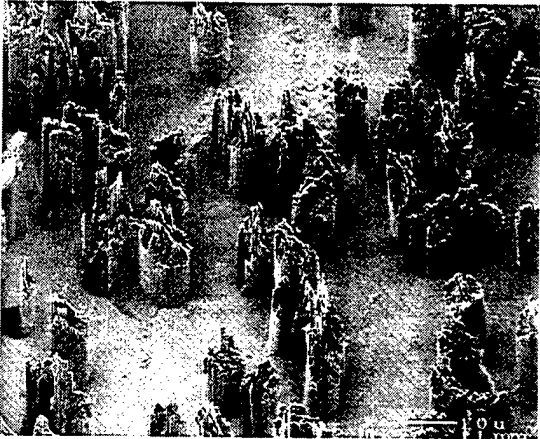
High resolution FE SEM examination of the transverse fracture surfaces of the fibers has provided valuable insight into the fibers' internal microstructures. Well-defined graphite sheet structures that protrude from the fracture surfaces indicate that all of the fibers are highly graphitized. There are, however, many differences between the microstructures of the three types of fibers that we studied: 1) the experimental fibers made from standard petroleum pitch precursor (P1 and P2), 2) the experimental fibers made from the experimental pitch precursor (E1 and E2), and 3) the K-1100 fibers. However, there was no distinguishable difference in the microstructures within either set of experimental fibers (P1 and P2, or E1 and E2), indicating that increasing the HTT from that of P2 and E2 to that of P1 and E1 does not affect the observed microstructure. Therefore, in comparing the microstructures of the standard precursor fibers to the experimental precursor fibers, fibers of either HTT can be used.

For each of the three fibers and the ThermalGraph® material, stereographic pairs of SEM photos have been included in Appendix A. By viewing a stereographic pair at the proper distance and focusing at infinity, the reader will see three images, the middle of which is a stereo image of the fracture surface. This process is facilitated by holding a piece of paper, such as a note card, between the two photos.

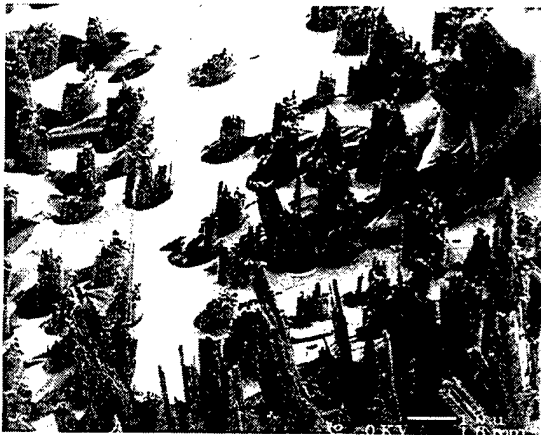
Figure 5 provides an overall view at low magnification of the fracture surfaces of the three types of fibers that were studied. Figures 6–8 show SEM photos of typical samples of the three types of fibers at significantly higher magnification. An important feature to note from Figs 5–8 is that all of the fibers are very well graphitized, as seen by the graphite sheets that protrude from the fracture surfaces. Comparing the two types of experimental fibers (Fig. 5(a) and (b)), much less pullout of graphitic planes is apparent in the standard precursor fibers (Fig. 5(a)) and, in many cases, a relatively flat fracture surface is observed. The experimental precursor fibers have fractured in a tougher, less-brittle fashion.



(a)



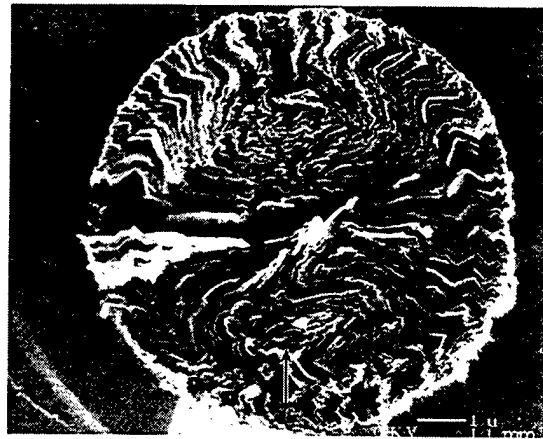
(b)



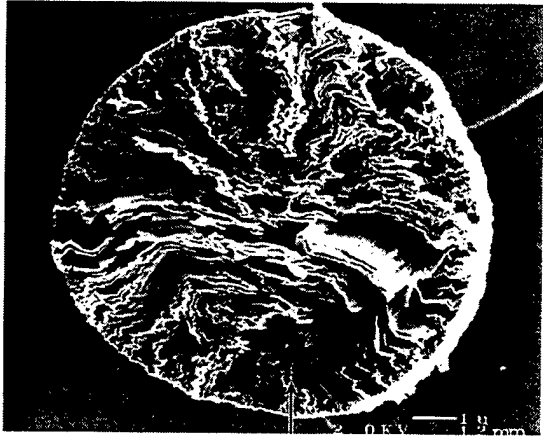
(c)

Fig. 5. FE SEM photomicrographs of fractured fibers. (a) Standard pitch precursor (P1), (b) experimental pitch precursor (E1), (c) K-1100.

resulting in more layer plane pullout. The layer planes are better defined, and the graphite sheets are clearly coarser (Fig. 5(b)). The K-1100 fibers also reveal tough fracture and significant pullout (Fig. 5(c)). However, compared to the experimental precursor fibers, the pullout in the K-1100 reveals an underlying microstructure that is more fibrillar than sheetlike.



(a)

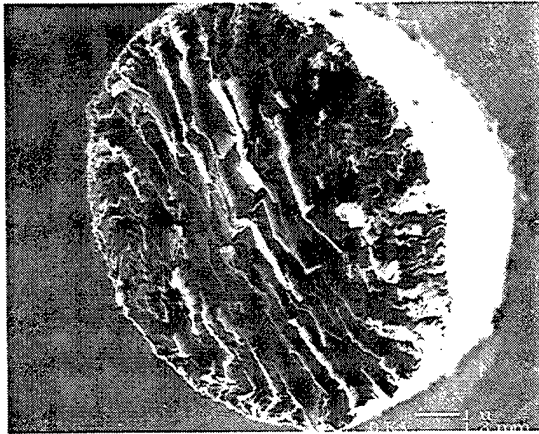


(b)

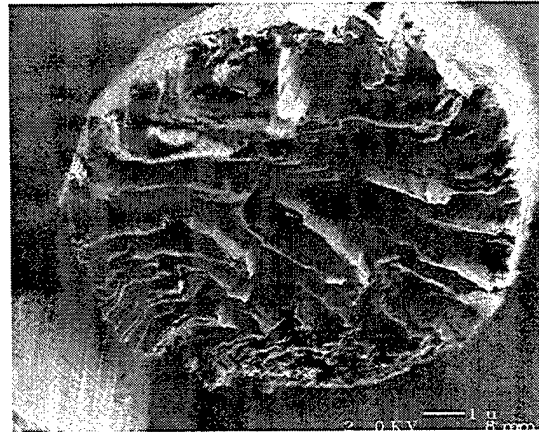
Fig. 6. FE SEM photomicrographs of the transverse fracture surfaces of standard pitch precursor fibers. (a) P1, (b) P2.

The K-1100 fibers shown in Figs 8(a) and (b) are essentially circular in cross section and have diameters of about 7 to 9  $\mu\text{m}$ . Both experimental fibers (Figs 6 and 7) are oval in cross section and have diameters of about 9 to 10  $\mu\text{m}$  in the long direction of the oval and about 7 to 8  $\mu\text{m}$  in the short direction. The open-wedge feature seen in the P1 fiber shown in Fig. 9 was seen in the K-1100, P1 and P2 fibers, and in the ThermalGraph<sup>®</sup> panel. None of the experimental precursor fibers observed had the open-wedge feature.

Most of the standard precursor fibers (Fig. 6) exhibit what could be termed a modified classical oriented core structure [22], with the layers in the core running parallel to the longer (equatorial) axis and being largely continuous from end to end. However, beyond the core, the layers in most cases bend very sharply toward the poles in a zig-zag pattern (radial zig-zag) while remaining essentially continuous from end to end. The severity of this layer plane bending is such that the layers almost fold back onto each other, resulting in a disordered enclosed zone where the layers have little continuity



(a)



(b)

Fig. 7. FE SEM photomicrographs of the transverse fracture surfaces of experimental pitch precursor fiber E2.

(arrows in Figs 6(a) and 6(b)). FitzGerald *et al.* [22] have illustrated schematically the structure of one type of oriented core fiber (based on observations of Amoco high modulus P-type fibers) containing three distinct zones: 1) the equatorial oriented core, 2) a transitional zone between the core and the two polar zones, and 3) a disordered zone at the polar regions. This description differs from what was observed here with the P1 and P2 fibers, in that the layers in the transitional zone bend much more severely, and the disordered region is not located at the poles, but rather, in this enclosed loop formed by the sharp curvature of the layers in the transitional zone.

The experimental precursor fibers (Fig. 7) also show a well-oriented core, but the core is significantly larger than in the standard precursor fibers. In the experimental precursor fibers, the core is so large that there is little or no transitional zone. The noncore region is essentially radially oriented. However, its principal feature is the degree of disorder as measured by the graphite planes folding back on each other over very short distances to form closed loop structures. These structures often appear as scrolls or have



(a)

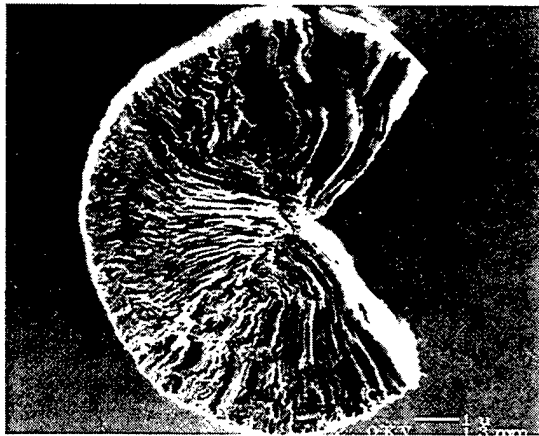


(b)

Fig. 8. FE SEM photomicrographs of the transverse fracture surfaces of K-1100 fibers.

triangular and even rectangular cross sections. Scroll structures in these fibers are shown by the arrows in the higher magnification SEM photo in Fig. 10.

We also see an interesting corrugation effect in the larger layers in the core when they are well exposed (as at 9 o'clock in the fiber in Fig. 7(b)), with corrugated "ribs" running parallel to the fiber axis. This corrugation was found in all of the fibers that were examined and has been reported by a number of other workers [10,23 25]. It is the result of a *regular* cyclical folding of the layers. That is, the amplitude and angle of folding are essentially constant, while the spacing between folds, or corrugations, is generally not constant. Figure 11(a) illustrates this point with a high magnification view of a P2 fiber end showing two folded layers, labeled A and B. Note that the regularity of folding in the corrugated layer A results in the layer effectively traversing its distance without changing direction. This is in contrast to layer B, where the folding is irregular and the layer zig-zags as it traverses its distance. Layer B can be thought of as a randomly folded, or kinked, layer. A corrugated area of fiber E1 is shown in Fig. 11(b).

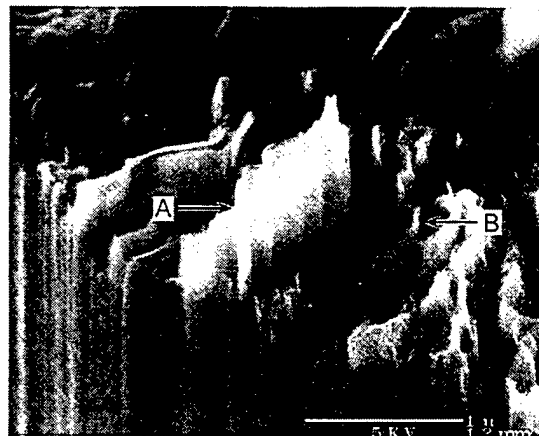


(a)



(b)

Fig. 9. FE SEM photomicrographs of the open-wedge feature in fiber P1.



(a)



(b)

Fig. 11. FE SEM photomicrographs of the corrugated structure. (a) fiber P2, (b) fiber E1.

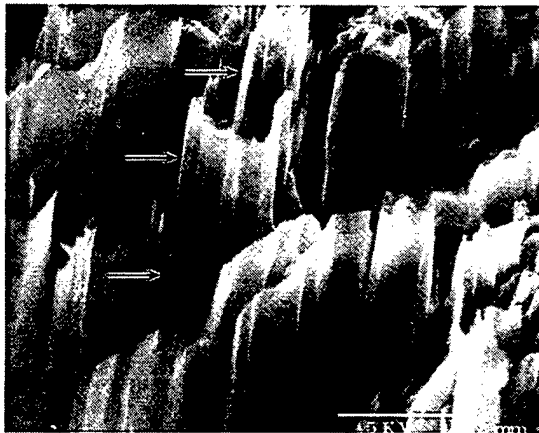


Fig. 10. FE SEM photomicrograph of the scroll structure in fiber E2.



Fig. 12. FE SEM photomicrograph of the K-1100 fiber core.

The K-1100 fibers reveal another modification of the oriented core structure in that the layers in the center of the fiber are highly convoluted, twisting and turning back on themselves to often form distinct "Y" and "V" shaped patterns. This convolution is seen clearly in Fig. 12, which is a high magnification

photo of the center of the fiber shown in Fig. 8(b). Aside from this convoluted core, the structure of K-1100 fibers is very similar to that of fibers P1 and P2.

SEM photos of transverse fracture surfaces of the ThermalGraph<sup>®</sup> material are presented in Figs 13 and 14. (A stereo pair is shown in Appendix A.)

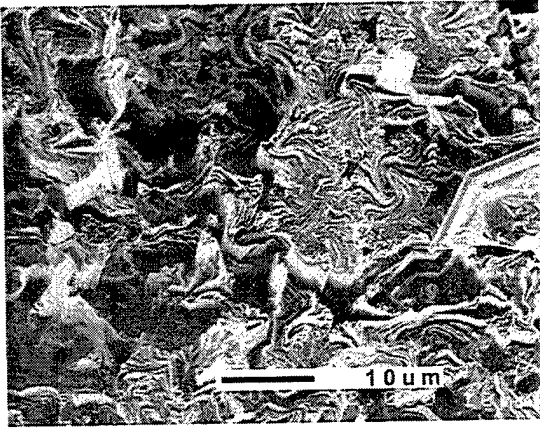


Fig. 13. FE SEM photomicrograph of the transverse fracture surface of ThermalGraph<sup>®</sup> panel.



Fig. 14. FE SEM photomicrograph of the transverse fracture surface of ThermalGraph<sup>®</sup> panel.

Figs 13 and 14 reveal two very important features of this material. The first is the very obvious fusion of the fibers. This feature is particularly clear in Fig. 13. Nevertheless, fiber remnants are nearly always evident, as seen clearly in Fig. 14. The net result of this fiber fusion is a continuous, or "self-reinforced", graphite structure, although with a significant amount of porosity. The second feature is the extent to which the ThermalGraph<sup>®</sup> differs in microstructure from the parent pitch fibers. As noted previously, the center region of the K-1100 fibers is typically highly convoluted, so that there is little or no layer plane continuity through the core region. In contrast, the layers in the core regions of the ThermalGraph<sup>®</sup> typically run completely through the remnant fibers in a swirling S-shaped manner, as seen in Fig. 14. In Fig. 14, the large oval-shaped fiber in the lower left of the photo has large kinked (but not convoluted) layers traversing the short diameter of the oval. This highly kinked core structure departs significantly from that found in the classical oriented core fiber. At the top of this fiber (12 o'clock), the layers continue through the fine structured region at

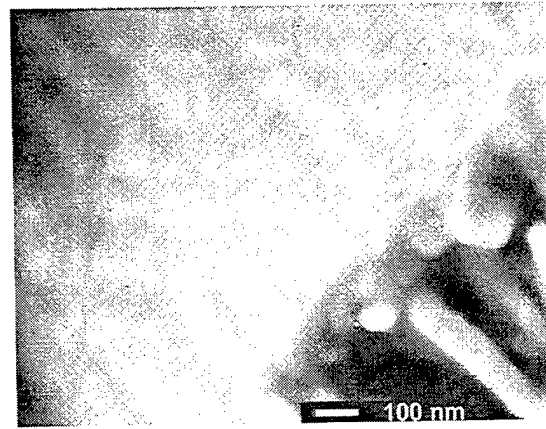


Fig. 15. FE SEM photomicrograph of the exposed fiber surface in ThermalGraph<sup>®</sup> panel.

the fiber perimeter and proceed to coarsen again as they move beyond the perimeter into the adjacent fiber remnant. We believe that the coarser microstructure in the ThermalGraph<sup>®</sup> is the result of not constraining the layer planes as occurs during typical fiber processing.

The longitudinal surface of a fiber remnant is seen in Fig. 15. The fine structure seen on the longitudinal surface is essentially identical to that first observed by Yoon and coworkers [26-28] on a variety of mesophase pitch fibers. Following their terminology, the surface consists of "fibrils" aligned along the fiber axis and "pleat units" on each fibril running perpendicular to the fibrils and the fiber axis. They observed the presence of fibrils and pleat units on fibers derived from a number of petroleum and synthetic precursors heat treated to 2400°C and on a coal-tar pitch fiber that was only carbonized, thereby showing that graphitization heat treatment was not necessary for fibril and pleat structure development [26]. Neither fibrils nor pleats were observed on PAN-based fibers or fibers derived from isotropic pitch. This observation led these workers to conclude that the fibril and pleat structures were characteristic of the liquid crystalline nature of the mesophase state. They speculate that microdomains in the mesophase, formed by a clustering of constituent molecules, are the precursors for the fibril and pleat microstructural units, and that the shape and dimensions of the fibrils and pleats are influenced by both spinning conditions and the mesophase precursor.

Robinson and Edie [25] have also observed fibril and pleat structures on three experimental ribbon-shaped fibers that differed in mesophase precursors (petroleum pitch versus naphthalene pitch) and in capillary entry design (flat entry versus profiled entry). However, high resolution SEM photos taken of the longitudinal surface of one of the fibers at some distance (not specified) away from the fracture surface were less definitive in resolving the pleat units, although they revealed a bumpy, nodular sur-



Fig. 16. FE SEM photomicrograph of the K-1100 fiber surface.

face that was at least suggestive of the better defined pleats seen in other photos. Robinson and Edie suggest that the pleat structure might be an artifact of fracture rather than a true structural unit. However, based on our observation in Fig. 15, where the pleats are seen at  $\sim 1$  to  $1.5 \mu\text{m}$  from the fracture surface, and the observations of Yoon and coworkers, it is difficult to imagine how the fracture process could create the pleat units.

We looked at the pleat units in more detail in the various fibers. Figure 16 is a SEM photo of a K-1100 fiber at the same magnification as that of the ThermalGraph<sup>®</sup> specimen seen in Fig. 15. The longitudinal surface reveals pleat-like units, but they are much less uniform and frequent than those in Fig. 15. It is important to note, however, that since the fibers were embedded in a carbon matrix when they were fractured, only those fibers were visible that pulled out due to the fracture and, therefore, protruded above the composite fracture surface (see Fig. 5). This means that the longitudinal surface could have been affected by the presence of the resin-based carbon matrix, either by the matrix adhering to the fiber or by damaging the surface as the fiber was pulled through the well-bonded matrix.

Figure 17(a) and (b) show the interior of a fractured K-1100 fiber. The two photos differ in that the operating voltage was 1 kV in Fig. 17(a) and 3 kV in Fig. 17(b). It can be seen that the use of the 3 kV voltage (Fig. 17(b)) results in excellent definition of pleat structures in the fractured segment in the middle of the photo (indicated by the arrow), whereas 1 kV fails to provide the same definition. A higher magnification view of this segment at 2 kV is seen in Fig. 18 (sample is rotated). The important conclusion to be drawn is that the observation of fine microstructural features in the fibers, such as pleat units, is very sensitive to the SEM operating parameters.

The surface of the designated segment in Figs 17 and 18, unlike the surface of the fiber in Fig. 15, is



(a)



(b)

Fig. 17. FE SEM photomicrograph of the internal surfaces of the K-1100 fiber. (a) 1 kV electron beam voltage, (b) 3 kV electron beam voltage.

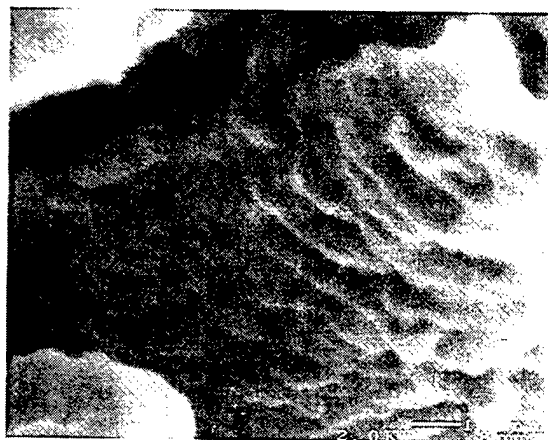


Fig. 18. FE SEM photomicrograph of the internal surface of the K-1100 fiber at higher magnification and 2 kV electron beam voltage.

most probably a fracture surface produced and exposed by pullout accompanying the fracture of the fiber. Therefore, for such an interior fracture surface,

the argument that the pleat units are an artifact of the fracture cannot be dismissed. Nevertheless, as we saw for the experimental precursor fibers, the fracture process was responsible for revealing the large layer planes that were clearly characteristic of this fiber. In the same way, it seems reasonable to us that the pleats observed in Figs 17 and 18 are an inherent microstructural feature of the fiber. We would also expect the fracture process to create more irregular patterns than those on the unfractured surfaces. Therefore, we concur with Yoon and coworkers that the pleats, when seen in mesophase fibers, are indeed a genuine microstructural feature and not an artifact of fracture.

As stated above, the most striking feature revealed by the high resolution SEM photomicrographs is the high degree of graphitization of all of the samples examined. There are indeed differences observed in the microstructures of the fibers made from standard precursor and those made from experimental precursor. However, there are no obvious features visible in the micrographs that would explain the significant differences in the thermal conductivity between fibers of the same precursor at different HTTs. It appears that SEM has limited sensitivity in this regard. This is not surprising, since XRD shows that the changes that are occurring take place at the atomic level and, therefore, are too fine to be resolved by SEM. The microstructural features that we have observed are formed predominantly while the materials are in the plastic mesophase state. In contrast to these gross microstructural changes, nanometer-scale atomic ordering occurs at much higher HTTs.

## 5. SUMMARY AND CONCLUSIONS

The microstructures of five high thermal conductivity mesophase-based graphite fibers and a self-reinforced graphite panel were characterized by XRD and high resolution FE SEM. The low  $d$ -spacings, narrow peaks and presence of three-dimensional ( $hkl$ ) reflections found in the XRD patterns of the five fibers and the ThermalGraph<sup>®</sup> panel indicate that they are all highly graphitic. The thermal conductivities of these materials correlate best with the graphite inter-basal-plane spacing ( $d_{002}$ ) as measured by XRD. The XRD data also indicate that at the same HTT, the fibers produced from the experimental precursor are more graphitic than those produced from the standard precursor.

The major result of the high resolution SEM examination of the ThermalGraph<sup>®</sup> panel is the evidence that the precursor fibers have coalesced into a continuous three-dimensional structure. The result of this fiber fusion is a "self-reinforced", graphitic structure.

The high resolution FE SEM micrographs of mesophase-based carbon fibers reveal many detailed microstructural features. All of the fibers appear very

graphitic. Well-developed graphene layer planes in the fibers that would be unresolvable by polarized-light optical microscopy were clearly seen. However, there are no obvious features visible in the micrographs that would explain the significant differences in thermal conductivity between fibers of the same precursor at different HTTs. SEM was found to have limited sensitivity in this regard.

*Acknowledgements* We would like to thank the Office of Naval Research for funding this work. Mr Albert Bertram of the Naval Surface Warfare Center, Carderock Division, was the technical monitor. Drs G. W. Ward and G. V. Deshpande of Amoco Performance Products, Inc., provided the fiber samples, and Mr W. C. Riley of Research Opportunities, Inc., provided the ThermalGraph<sup>®</sup> sample. We would also like to thank Drs R. Bacon and B. J. Sullivan for many helpful suggestions during the course of this research and Ms J. Naiditch for her masterful editing.

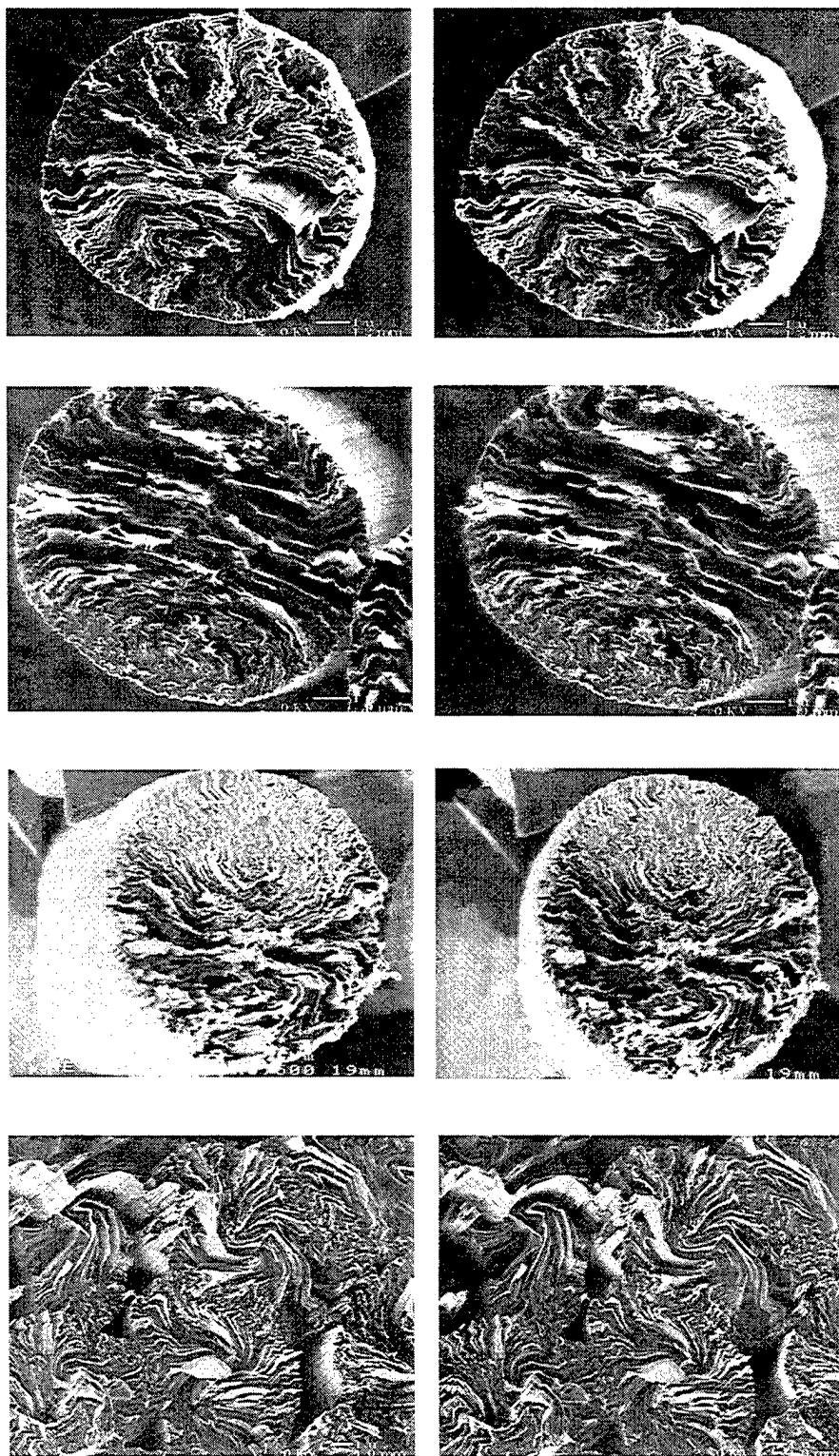
## REFERENCES

- Schulz, D. A. and Nelson, L. C., US Patent No. 5,266,294, 1993.
- Barr, J. B., Hecht, D. H. and Levan, C. D., High thermal conductivity panels from mesophase pitch fibers, in *Extended Abstracts 22nd Biennial Conference on Carbon*, 1995, pp. 32-33.
- Riley, W. C., private communication.
- Bish, D. L. and Reynolds, Jr, R. C., Sample preparation for X-ray diffraction, in *Modern Powder Diffraction: Review in Mineralogy*, Vol. 20, ed. D. L. Bish and J. E. Post. Mineralogical Society of America, Washington, DC, 1989, pp. 73-97.
- Aladekomo, J. B. and Bragg, R. H., *Carbon*, 1990, **28**, 897.
- Bragg, R. H. and Aladekomo, J. B., *J. Appl. Cryst.*, 1995, **28**, 14.
- Klug, H. P. and Alexander, L. E., *X-ray Diffraction Procedures*. John Wiley, New York, 1974.
- Anderson, D. P., Carbon fiber morphology, II: expanded wide angle X-ray diffraction studies of carbon fibers. WRDC-TR-90-4137, Wright Patterson AFB, OH, 1991.
- Mallon, J. J. and Adams, P. M., *Mol. Cryst. Liq. Cryst.*, 1993, **231**, 69.
- Vezie, D. L. and Adams, W. W., *J. Mater. Sci. Lett.*, 1990, **9**, 883.
- Zaldivar, R. J., Rellick, G. S. and Yang, J. M., *J. Mater. Res.*, 1993, **8**, 501.
- Zaldivar, R. J. and Rellick, G. S., *Carbon*, 1991, **29**, 1155.
- Zaldivar, R. J., Rellick, G. S. and Yang, J. M., *SAMPE J.*, 1991, **27**, 29.
- Nysten, B., Issi, J. P., Barton, R., Boyington, D. R. and Lavin, J. G., *Phys. Rev. B*, 1991, **44**, 2142.
- Kelly, B. T., *Carbon*, 1967, **5**, 247.
- Kelly, B. T., *Carbon*, 1968, **6**, 71.
- Kelly, B. T., *Carbon*, 1968, **6**, 485.
- Kelly, B. T., *Chemistry and Physics of Carbon*, Vol. 5, ed. P. L. Walker, Jr. Dekker, New York, 1969, p. 119.
- Bowman, J. C., Krumhansl, J. A. and Meers, J. T., *Industrial Carbon and Graphite Society of Chemical Industry*, London, 1958, p. 52.
- Heremans, J., Rahim, I. and Dresselhaus, M. S., *Phys. Rev. B*, 1985, **32**, 6742.
- Amoco unpublished data.
- FitzGerald, J. D., Pennock, G. M. and Taylor, G. H., *Carbon*, 1991, **29**, 139.
- Roche, E. J., *J. Mater. Sci.*, 1990, **25**, 2149.

24. Endo, M., *J. Mater. Sci.*, 1988, **23**, 598.
25. Robinson, K. E. and Edie, D. D., *Carbon*, 1996, **34**, 13.
26. Yoon, S.-H., Korai, Y. and Mochida, I., *Carbon*, 1994, **32**, 1182.
27. Yoon, S.-H., Korai, Y., Mochida, I., Yokogawa, K., Fukuyama, S. and Yoshimura, M., *Carbon*, 1996, **34**, 83.
28. Mochida, I., Yoon, S.-H., Takano, N., Fortin, F., Korai, Y. and Yokogawa, K., *Carbon*, 1996, **34**, 941.

## APPENDIX A

- A(a). Stereo photomicrographs of the transverse fracture surface of fiber P2.  
A(b). Stereo photomicrographs of the transverse fracture surface of fiber E2.  
A(c). Stereo photomicrographs of the transverse fracture surface of K-1100 fiber.  
A(d). Stereo photomicrographs of the transverse fracture surface of ThermalGraph<sup>30</sup> panel.



## TECHNOLOGY OPERATIONS

The Aerospace Corporation functions as an "architect-engineer" for national security programs, specializing in advanced military space systems. The Corporation's Technology Operations supports the effective and timely development and operation of national security systems through scientific research and the application of advanced technology. Vital to the success of the Corporation is the technical staff's wide-ranging expertise and its ability to stay abreast of new technological developments and program support issues associated with rapidly evolving space systems. Contributing capabilities are provided by these individual Technology Centers:

**Electronics Technology Center:** Microelectronics, VLSI reliability, failure analysis, solid-state device physics, compound semiconductors, radiation effects, infrared and CCD detector devices, Micro-Electro-Mechanical Systems (MEMS), and data storage and display technologies; lasers and electro-optics, solid state laser design, micro-optics, optical communications, and fiber optic sensors; atomic frequency standards, applied laser spectroscopy, laser chemistry, atmospheric propagation and beam control, LIDAR/LADAR remote sensing; solar cell and array testing and evaluation, battery electrochemistry, battery testing and evaluation.

**Mechanics and Materials Technology Center:** Evaluation and characterization of new materials: metals, alloys, ceramics, polymers and composites; development and analysis of advanced materials processing and deposition techniques; nondestructive evaluation, component failure analysis and reliability; fracture mechanics and stress corrosion; analysis and evaluation of materials at cryogenic and elevated temperatures; launch vehicle fluid mechanics, heat transfer and flight dynamics; aerothermodynamics; chemical and electric propulsion; environmental chemistry; combustion processes; spacecraft structural mechanics, space environment effects on materials, hardening and vulnerability assessment; contamination, thermal and structural control; lubrication and surface phenomena; microengineering technology and microinstrument development.

**Space and Environment Technology Center:** Magnetospheric, auroral and cosmic ray physics, wave-particle interactions, magnetospheric plasma waves; atmospheric and ionospheric physics, density and composition of the upper atmosphere, remote sensing, hyperspectral imagery; solar physics, infrared astronomy, infrared signature analysis; effects of solar activity, magnetic storms and nuclear explosions on the earth's atmosphere, ionosphere and magnetosphere; effects of electromagnetic and particulate radiations on space systems; component testing, space instrumentation; environmental monitoring, trace detection; atmospheric chemical reactions, atmospheric optics, light scattering, state-specific chemical reactions and radiative signatures of missile plumes, and sensor out-of-field-of-view rejection.